journal of the mechanical behavior of biomedical materials 103 (2020) 103557

Contents lists available at ScienceDirect

Journal of the Mechanical Behavior of Biomedical Materials

journal homepage: http://www.elsevier.com/locate/jmbbm

3D-additive deposition of an antibacterial and osteogenic silicon nitride coating on orthopaedic titanium substrate

Matteo Zanocco [a,b], Francesco Boschetto [a,b], Wenliang Zhu [a], Elia Marin [a,c], Bryan J. McEntire [d], B. Sonny Bal [d], Tetsuya Adachi [c], Toshiro Yamamoto [c], Narisato Kanamura [c], Eriko Ohgitani [b], Kengo Yamamoto [e], Osam Mazda [b], Giuseppe Pezzotti [a,b,e,f,*]

[a] Ceramic Physics Laboratory, Kyoto Institute of Technology, Sakyo-ku, Matsugasaki, Kyoto, 606-8585, Japan
[b] Department of Immunology, Graduate School of Medical Science, Kyoto Prefectural University of Medicine, Kamigyo-ku, 465 Kajii-cho, Kyoto, 602-8566, Japan
[c] Department of Dental Medicine, Graduate School of Medical Science, Kyoto Prefectural University of Medicine, Kamigyo-ku, Kyoto, 602-8566, Japan
[d] SINTX Technologies Corporation, 1885 West 2100 South, Salt Lake City, UT, 84119, USA
[e] Department of Orthopedic Surgery, Tokyo Medical University, 6-7-1 Nishi-Shinjuku, Shinjuku-ku, 160-0023, Tokyo, Japan
[f] The Center for Advanced Medical Engineering and Informatics, Osaka University, 2-2 Yamadaoka, Suita, Osaka, 565-0854, Japan

A B S T R A C T

A 3D-additive manufacturing approach produced a dense Si_3N_4 ceramic coating on a biomedical grade commercially pure titanium (cp-Ti) substrate by an automatic laser-sintering procedure. Si_3N_4 coatings could be prepared with thicknesses from the single to the tens of microns. A coating thickness, $t = 15 \pm 5$ μm, was selected for this study, based on projections of homogeneity and scratching resistance. The Si_3N_4 coating met the 20 N threshold required for biomaterial applications, according to the standard scratch testing (ASTM C1624-05). The Si_3N_4 coating imparted both the antibacterial and osteogenic properties of bulk Si_3N_4 to the cp-Ti substrate. Both properties were comparable to those previously described for bulk Si_3N_4 biomedical implants. The newly developed Si_3N_4-coating was applied to commercially available Ti-alloy acetabular shells for total hip arthroplasty. A "glowing" test based on luciferase gene transformation was applied to visualize the colonization of gram-negative *Escherichia coli* on Si_3N_4-coated and uncoated Ti-alloy acetabular shells. The results showed that the coating technology conferred resistance to *Staphylococcus epidermidis* and *Escherichia coli* adhesion onto the bulk acetabular sockets.

1. Introduction

In prosthetic joint replacement, most notably total hip and knee replacements, osseous fixation of implants through direct bone ingrowth (i.e., cementless fixation) is preferred, usually with a layer of porous Ti6Al4V alloy (referred to as Ti-alloy, henceforth) (Karuppal, 2016). Mechanical fixation through a scratch-fit avoids implant micromotion, while host bone gains ingrowth into the porous Ti-alloy layer to achieve long-term durable implant stability (Wang et al., 2013). Various enhancements to the porous surface configuration of Ti-alloy, including 3D-printing methods (Homsy et al., 1972), have been described to promote implant osteointegration (Karuppal, 2016; Marin et al., 2010). A pore size of 50–400 μm is considered optimal for bone ingrowth (Anselme, 2000). Reliable, long-term implant fixation by direct bone attachment to arthroplasty implants can be achieved with porous Ti-alloy (Hailer et al., 2010).

From a chemical standpoint, an nm-sized passivation layer (mainly titanium oxide) at the surface of Ti-alloy facilitates the adhesion of osteoblasts, thereby promoting implant fixation to living bone. However, the process is not always successful, if instead of bony fixation fibrosis develops between the bone and implant surface. The resulting micromotion can lead to pain and the release of toxic metallic ions at the bone/implant interface (Marin et al., 2010; Chassot et al., 2004; Apostu et al., 2018).

In addition to the failure of bone ingrowth into porous Ti-alloy, periprosthetic infection can also lead to revision, i.e., repeat surgery in joint replacements. The combined incidence from these mechanisms was 7–16%, according to Finnish and Danish registry data up to the 2001 (Puolakka et al., 2001; Lucht, 2000). Higher fractions (19–40%) have been reported for patients with degenerative arthritis (depending on age and sex), according to 2013–2017 data from the Canadian registry (Canadian Institute for Health Information, 2018). Cementless fixation may itself be protective against infection risk. The incidence of periprosthetic infections with cementless Ti-alloy implants after short-term implantation was about half that for other types of implants, according to the Norwegian Arthroplastic Registry for the period 1987–2003

* Corresponding author.Ceramic Physics Laboratory, Kyoto Institute of Technology, Sakyo-ku, Matsugasaki, Kyoto, 606-8585, Japan.
E-mail address: pezzotti@kit.ac.jp (G. Pezzotti).

https://doi.org/10.1016/j.jmbbm.2019.103557
Received 29 June 2019; Received in revised form 7 November 2019; Accepted 25 November 2019
Available online 26 November 2019
1751-6161/© 2019 Published by Elsevier Ltd.

(Engesæter et al., 2006). The lack of cement in the total hip joint construct may contribute to a decreased risk of infection (Engesæter et al., 2006). One mechanism for this observation may be the passivation layer on Ti-alloy that partly counteracts bacterial colonization. Electron-hole pairs trapped at the surface layer of oxidized TiO_2 have strong reducing and oxidizing properties. Their reaction with H_2O or hydroxide ions generates hydroxyl radicals (OH) and superoxide ions (O_2) that attack polyunsaturated phospholipids in the bacterial membrane and catalyze site-specific damages in their DNA (Maness et al., 1999; Hirakawa et al., 2004). Even with this inherent antibacterial mechanism on Ti surfaces, periprosthetic infection remains a concern, and is a leading cause of repeat surgery in joint replacement.

In sum, improvements to both the osteogenic capability of porous Ti-alloy, as well as its ability to resist bacterial adhesion are warranted in order to reduce the incidence of failed cementless total hip and total knee arthroplasty. Such improvements are particularly relevant with the current emphasis on rapid recovery from surgery, faster return to function, and outcome measures that influence surgeon/institutional reimbursement, especially in the United States.

Our hypothesis was that multifunctional Si_3N_4 coating would concurrently enhance osteogenesis and discourage bacterial adhesion when applied to porous Ti-alloy. Recent work has shown that Si_3N_4 surfaces express reactive nitrogen species (RNS) that promote cell differentiation and osteogenesis (Pezzotti et al., 2016a, 2016b, 2017a, 2017b, Pezzotti, 2019), while resisting both gram-positive and gram-negative bacteria (Pezzotti et al., 2016c, 2018). Bulk Si_3N_4 implants are used in spinal fusion surgery (Rambo, 2018; Smith et al., 2018; Ball et al., 2017). The dual advantage of RNS in terms of promoting osteogenesis, while discouraging bacterial proliferation has been shown in animal studies (Webster et al., 2012) and advanced spectroscopic analyses on a retrieved human spinal implant have shed light on the mechanism of enhanced osteogenesis of Si_3N_4 (Pezzotti et al., 2017c; Pezzotti, 2019).

In this paper, we describe a novel method of depositing a micrometer thick Si_3N_4 layer on anodized Ti-alloy using an automatic 3D-additive laser-sintering procedure. We tested scratching resistance of this coating and validated its osteogenic and antibacterial properties *in vitro*, with uncoated Ti-alloy and bulk Si_3N_4 serving as negative and positive controls, respectively. We demonstrated commercial feasibility of this technology by applying the Si_3N_4 coating to commercially available Ti-alloy sockets, and testing their bacterial resistance *in toto*.

2. Experimental procedures

2.1. Si_3N_4-coating fabrication and characterizations

The starting micrometric powder used for laser-sintering the Si_3N_4 coating consisted of a 90 wt% fraction of β-Si_3N_4 (SINTX Co., Salt Lake City, UT, USA) mixed with 6 wt% yttrium oxide (Y_2O_3, Grade C, H.C. Starck, Munich, Germany) and 4 wt% aluminium oxide (Al_2O_3, SA8-DBM, Baikowski/Malakoff, Charlotte, North Carolina) (McEntire et al., 2016). We used a Vision LWI VERGO-Workstation equipped with a Nd:YAG laser with a wavelength of 1064 nm (max pulse energy: 70 J, peak power 17 kW, voltage range 160–500 V, pulse time 1–20 ms, spot size 250–2000 μm) to achieve densification of successive layers of Si_3N_4 powder placed on the water-wet surface of the Titanium substrate. The apparatus operated under a constant flux of nitrogen gas flow in order to limit Si_3N_4 decomposition and oxidation. The Nd:YAG laser was pulsed with a spot size of 2 mm, driven by an applied voltage of 400 V, and with a pulse time of 4 ms. The operation was repeated until obtaining a continuous thickness, $t = 15 \pm 5$ μm, over the entire surface of the Titanium substrate. Squared 1 cm × 1 cm (0.5 cm thickness) samples were used for all the experiments. The fabrication procedure of the Si_3N_4 coating is schematically depicted in Fig. 1.

Cross-section crystallographic analyses were performed into a scanning electron microscope (SEM) equipped with an Electron-Backscattered X-ray Diffraction (EBSD) detector. The microhardness was then tested using a DUH-211S dynamic ultra-micro hardness tester (Shimadzu) with a triangular diamond tip and maximum applied force of 60 mN.

Scratch testing was performed on coated Titanium substrates according to the ASTM C1624-05 Standard (reapproved in 2010) using a diamond stylus with a conical Rockwell geometry (included angle 120° and tip radius equal to 200 μm). A progressively increasing vertical force was applied from 0.5 up to 25 N.

The same procedure used for coating Ti-alloy substrates was applied to coat *in toto* commercially available acetabular shells (G7® OsseoTi Limited; Zimmer Biomet, Warsaw, IN, USA); uncoated components served as controls ($n = 3$ per group). The hip components were made of Ti-alloy and possessed a porous surface morphology appropriated for cementless socket fixation to the pelvis (i.e., with a pore size in the order of 1 mm).

The surface morphology of the porous Ti-alloy acetabular shells before and after laser Si_3N_4-coating was characterized with a confocal

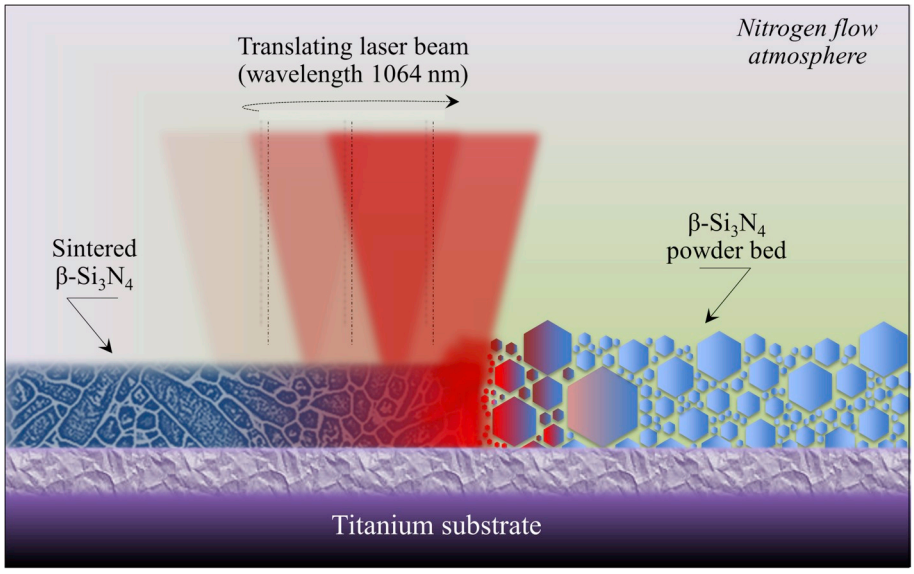

Fig. 1. Schematic draft of the 3D-additive laser-sintering fabrication procedure proposed for producing a dense Si_3N_4 ceramic coating on Titanium substrate.

scanning laser microscope (Laser Microscope 3D and Profile measurements, Keyence, VKx200 Series, Osaka, Japan) capable of high-resolution optical images with depth selectivity. All images were collected using 20x magnification. Scanning Electron Microscopy (SEM) and Energy Dispersive X-ray Spectroscopy (EDS) (JSM-700 1F, JEOL, Tokyo, Japan) were used to acquire high resolution images and chemical composition maps of both cross-sections and top-surface of Si_3N_4-coated substrates after scratch testing. Cross-sections were obtained by diamond-blade cutting and successive fine polishing with diamond paste.

2.2. Osteoconductivity test

SaOS-2 human osteosarcoma cells were cultured and incubated in 4.5 g/L glucose DMEM (D-glucose, L-Glutamine, Phenol Red, and Sodium Pyruvate; Nacalai Tesque, Kyoto, Japan) supplemented with 10% fetal bovine serum. The cells were then allowed to proliferate within petri dishes for about 24 h at 37 °C. After adjusting the final cell concentration at 5×10^5 cell/ml, the cultured cells were deposited on the surface of Si_3N_4-coated and uncoated Titanium substrates ($n = 3$ each type) previously sterilized by exposure to UV light. In osteoconductivity tests, cell seeding was performed in an osteogenic medium, which consisted of DMEM supplemented with about 50 μg/mL ascorbic acid, 10 mM β-glycerol phosphate, 100 mM hydrocortisone, and ~10% fetal bovine calf serum. The samples were incubated up to 7 days at 37 °C. The medium was changed twice during the week of incubation. Immunocytostaining was performed as the following. SaOS-2 were fixed with 4% paraformaldehyde for 15 min followed by 30 min incubation at room temperature with the following primary antibodies: mouse anti-human Gla osteocalcin (TakaraBio, Kusatsu-shi, Japan) and rabbit anti-human osteopontin (dilution = 1:500) (IBL, Maebashi-Shi, Gunma, Japan). The cells were then incubated with fluorescence conjugated and secondary antibodies Goat anti-Mouse Antibody FITC Conjugated (Bethyl Laboratories, Montgomery, TX, USA) and Goat anti-Rabbit Antibody PE Conjugated and (1:200) (Thermo Fisher Scientific, Waltham, MA, USA). Cell nuclei were stained with stained with Hoechst 33342 (1:100) (Dojindo, Kumamoto-Shi, Japan). The staining was observed under a fluorescent microscope (BZX710; Keyence, Osaka, Japan). Confocal scanning laser microscopy images were obtained with a 3D laser confocal microscope (OLS4000-SAT; Olympus Co., Tokyo, Japan) in order to assess the volumetric amounts per unit area of bony hydroxyapatite (Hap) produced by the SaOS-2 cells in one week. The amounts of osteocalcin and osteopontin in the deposited bony tissue were also estimated by direct pixel counting on fluorescence micrographs using automatic software.

2.3. Antibacterial tests

Freeze-dried pellets of *Staphylococcus epidermidis* (ATCCTM 14990®) (*S. epidermidis*, henceforth) were hydrated in heart infusion (HI) broth (Nissui, Tokyo, Japan) and incubated at 37 °C for 18 h in brain heart infusion (BHI) agar (Nissui). The mixture was subsequently assayed for colony forming units (CFU) and diluted to a concentration of 1×10^8 CFU mL^{-1} using phosphate-buffered saline (PBS). An aliquot of 100 μL of the bacterial suspension was spread onto individual BHI agar plates. The Si_3N_4 substrate samples (previously UV-sterilized) were then placed in contact with the agar for inoculation purposes, followed by incubation at 37 °C under aerobic conditions for 24 and 48 h.

Cell viability was evaluated by a tetrazolium-based assay using the Microbial Viability Assay Kit (WST-8; Dojindo). 24 and 48 h after cultivation, substrates with *Staphylococcus epidermidis* were collected and soaked in 1000 μL of PBS in 12-well plates. WST-8 solution was added to each wells and OD values measured (the absorbance at 490 nm) using plate reader EMax (molecular devices, San Jose, CA, USA) after incubation for 30–60 min.

At each time point, the test and control samples were observed by fluorescence microscopy (BZ-X700; Keyence, Osaka, Japan). For visualization, bacteria were stained with two different solutions: (i) 4′,6-diamidino-2-phenylindole (DAPI) which binds to and stains DNA blue thereby imaging the nucleus location; (ii) 5 (6)-carboxyfluorescein diacetate (CFDA; Dojindo, Kumamoto, Japan); and, (iii) propidium iodide (PI; Dojindo, Kumamoto, Japan). PI's red color highlighted dead or injured bacteria. Conversely, CFDA's green color revealed living bacteria. The staining protocol consisted of adding 1 μL of DAPI, the PI solution, and 15 μL of CFDA solution to the samples, and then incubating them for 5 min at 37 °C. After removing the buffer, the cells were analyzed under the fluorescence microscope. Quantitative assessments of the presence of living bacteria on the Si_3N_4 substrates were then directly obtained from automatic image analyses of the above micrographs by using >12 different fluorescence micrographs for each sample and $n = 3$ samples for each exposure-time condition.

Escherichia coli (25922 ®ATCC™) (*E. coli*, henceforth) was cultured at Kyoto Prefectural University of Medicine and the Dr. GENE 4: *E. coli* Transformation Kit (Toyo Ink Co. LTD. 4, Tokyo, Japan) was used to transform the vector (firefly luciferase gene) into *E. coli* cells. Previously sterilized by UV, Si_3N_4-coated and uncoated Ti-alloy acetabular shells ($n = 3$ each) were spread with the bacterial solution (1×10^8 CFU/mL) in brain heart infusion (BHI) agar (Nissui, Tokyo, Japan) at 37 °C. Incubation at 37 °C under aerobic conditions lasted for 48 h and the shell samples were successively subjected to luciferase firefly gene transformation. For doing so, a solution containing luciferin was added on the top of the acetabular shell samples. Upon reaction among adenosine triphosphate, Mg^{2+}, O_2, and luciferase enzyme, a "glowing" chemiluminescent signal could be captured by means of a CCD camera (ImageQuant LAS 500; GE Healthcare, Chicago, IL, USA) on the acetabular shell *in toto*, which revealed the presence of living bacteria.

2.4. Statistical analyses

Data relating to osteogenesis and antibacterial properties were analyzed by calculating their mean value ± one standard deviation. The Student's *t*-test was used to detect statistically significant differences between data, p values < 0.01 being considered statistically significant and labeled with two asterisks in the figures.

3. Experimental results

3.1. Structural, chemical, and mechanical characteristics of Si_3N_4 coating

Fig. 2 shows SEM/EDS analyses performed on the cross-section of a Si_3N_4-coated Ti-alloy substrate. The average thickness of the coating was $t = 15 \pm 5$ μm. The main feature in the SEM micrograph (a) is the wavy morphology of the ceramic/metal interface, which showed clear interlocks at the micrometer scale between metal and ceramic phases. Some residual porosity could have been retained in the coating, although it could not be directly observed neither by optical or by scanning electron microscopy. The rough surface morphology mainly arose from the inhomogeneous size of the silicon nitride powder (5 ÷ 50 μm). EDS elemental analyses of N, Si, and Ti (in (b), (c) and (d), respectively) revealed the presence of Nitrogen on both coating and substrate, Si-rich areas in coating area and no diffusional transport of the Ti element into the coating during laser sintering (the very weak Ti contamination in the coating area is believed to be an artifact of the cutting/polishing procedure applied to obtain the cross section). Unluckily, the low detectability of Nitrogen and the surface morphology of the coating make it impossible to quantify the amount of Nitrogen diffused in the substrate and the amount that was retained by the coating. However, it was clear that the treatment did not produce a TiN layer. On the other hand, the absence of Ti-element in the chemical composition of the coating shows that partial melting of the metallic alloy under the laser beam took place only in the immediate neighborhood of its surface (and was responsible for the wavy interface

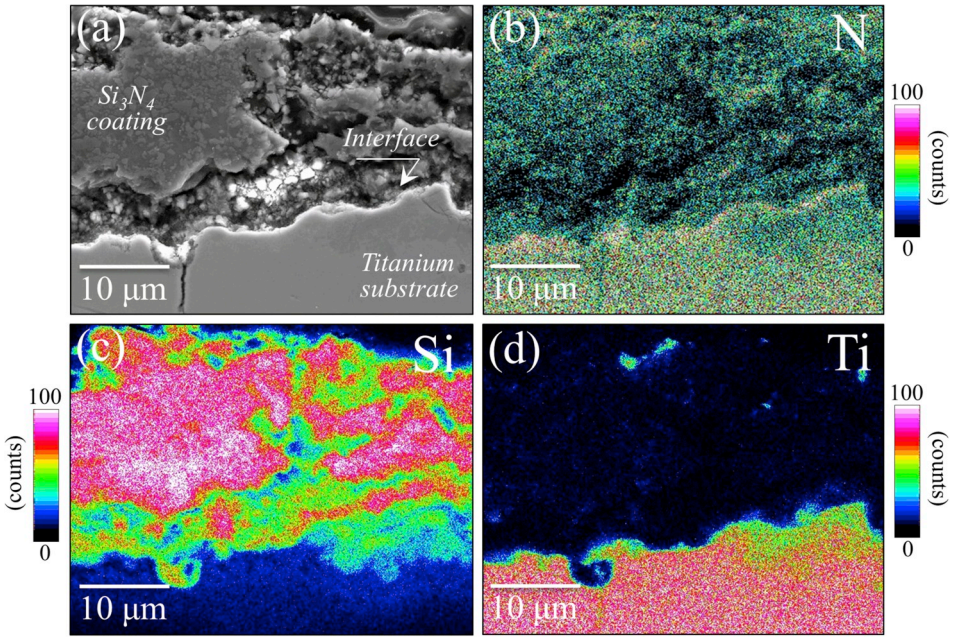

Fig. 2. SEM observation (a) and EDS analyses of N (b), Si (c), and Ti (d) elements on the cross-section of a Si_3N_4-coated Titanium substrate. Note the wavy morphology of the ceramic/metal interface with interlocks at the micrometer scale between.

morphology). A small area of relatively intense Titanium signal could be observed on the top of the coating in Fig. 2 (d). This is caused by splashes of molten titanium that occurred when the laser hit portions of substrate not completely covered by ceramic powder.

Fig. 3 shows the EBSD images of the cross section of the titanium samples coated with silicon nitride. Low magnification images, in Fig. 3 (a) and (b), show the grain structure and the orientation of the α-titanium phase down to about 200 μm in depth. As seen, during laser treatment, the titanium grains were affected and distorted by the heat treatment in the first 100 μm in depth, with the formation of crystal twinning, in particular in the region between 100 and 150 μm. Beyond 150 μm in depth, the microstructure was unaffected by the laser treatment. Fig. 3(c) and (d) show an area close to the Si_3N_4 interface at higher magnification. The titanium grains have an acicular shape with a preferential orientation orthogonal to the interface itself. The acicular region is followed by an area of elongated grains with a size comparable to the unaffected areas of Fig. 3(a) and (b). The black spot present on the images are intermetallic phases of titanium and silicon, which could not be identified by EBSD because of their wide range of stoichiometry.

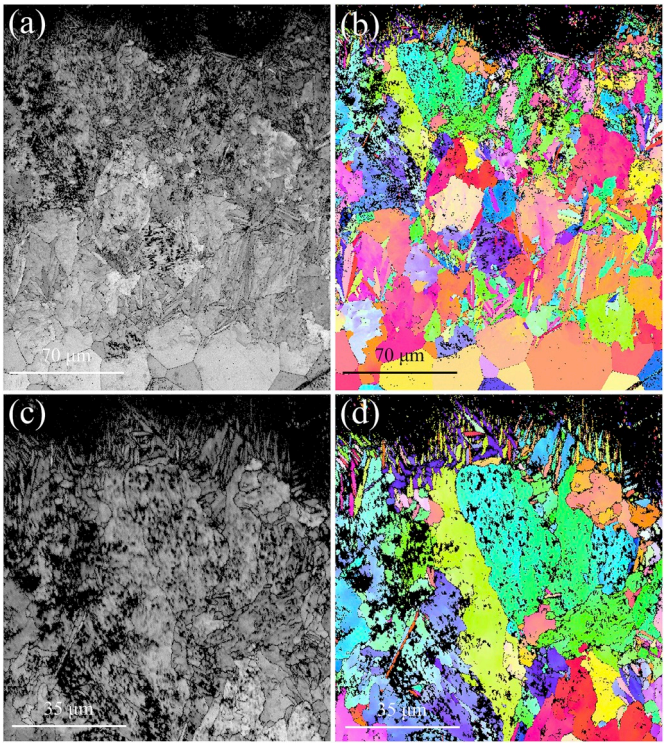

Fig. 3. Low (a) and (b), and high (c) and (d) magnification EBSD images taken in the neighborhood of the interface between coating and Titanium substrate to image size and orientation of the metal microstructure after laser treatment.

Fig. 4 shows the micro hardness results as obtained on a cross section of the sample. In particular, Fig. 4(a) shows three indentations performed at different distances from the interface with the coating. It can be observed that the first indentation on the left is smaller when compared with the other two, which have a similar size. Fig. 4(b) shows the average microhardness of the sample in the coating as a function of distance from the interface between coating and substrate. The microhardness of the coating could not be measures on the top surface due to roughness and inhomogeneities. The average value shown in the plot of Fig. 4(b) refers to measurements on the cross section. On the Titanium substrate, the hardness near the coated surface was higher as compared to the bulk material. This is mainly due to heating effect during the laser-fabrication of the coating. Local heating produced smaller grain and locally increased the hardness of the material.

Fig. 5(a) and (b) show low- and high-magnification SEM micrographs, respectively, taken on the top surface of the Si_3N_4 coating at the location where scratch testing was (progressively from left to right) applied with a load from 0 up to 25 N for a length about 1 mm. The scratch exerted by the conical diamond stylus introduced plastic deformation on the surface of Si_3N_4 coating. However, neither microcracks nor areas of spalling in the coating could be observed around the scratch, which demonstrates the high strength of attachment of the coating to the alloy substrate, thereby meeting the requirements of the ASTM C1624-05 Standard (requiring resistance up to 20 N) for biomaterials' applications. Elemental EDS analyses in Fig. 5(c), (d), and (e) show the distributions at the scratch site of N, Si, and Ti elements, respectively. The main feature in the EDS data was that no Ti contamination could be seen inside the scratched area, thus demonstrating that the running

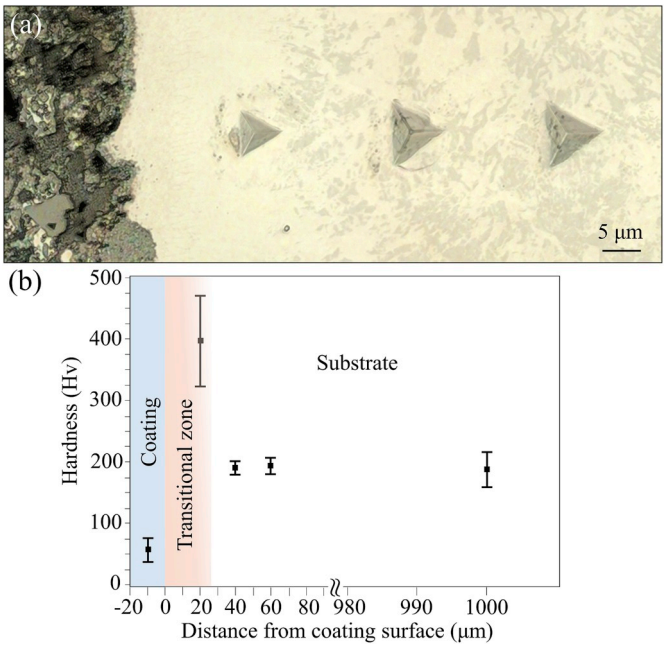

Fig. 4. Micro hardness indentation made on the cross section of the coating sample: (a) indentations performed on the cross-section, and (b) average hardness values as a function of distance from the interface between coating and substrate.

stylus did not reach the Ti-alloy layer at any load during testing. However, some local spot of Titanium element seen in Fig. 5 on the top surface of the coating likely arises from splashing of molten metal during laser treatment in areas not completely covered by Si_3N_4 powder.

3.2. Osteoconductivity of Si_3N_4 coating

Fig. 6(a) compares the volumetric amounts of bone tissue per unit area grown by SaOS-2 cells during 7 days of incubation as measured by laser microscopy on uncoated and Si_3N_4-coated Ti6Al4V substrates, in comparison with bulk Si_3N_4. In section (b) of the same figure, the composition of the bone tissue was evaluated with respect to its Gla-osteocalcin and osteopontin contents. Laser microscopy images for the uncoated alloy (Fig. 6(c) and (d)) and Si_3N_4-coated alloy (Fig. 6(e) and (f)) substrates are shown in planar and three-dimensional projections. A nearly homogeneous layer of bony apatite formed on the Si_3N_4-coated substrate, which reached a homogeneous layer of apatite profile with maximum height of ~50 μm. The total amount of hydroxyapatite (calculated over the entire substrate surface by exploiting an automatic software function available in the microscope) showed no statistically meaningful difference between the amounts of bone tissue grown by SaOS-2 cells on the Si_3N_4-coated alloy substrate and bulk Si_3N_4 under exactly the same testing conditions. Conversely, the amount of bone tissue grown on the Si_3N_4-coated Ti-alloy substrate was ~50% higher than that deposited by cells on the uncoated Ti-alloy substrate (cf. Fig. 6 (a)). Regarding the morphology of bone tissue deposition on this latter substrate, the SaOS-2 cells grew tissue only in very localized microscopic areas (cf. Fig. 6(c) and (d)), in which the height of the deposited apatite reached up to ~80 μm.

Additional experiments aimed at clarifying the composition of the bone tissue deposited by cells revealed that the fractions of Gla-osteocalcin and osteopontin (given as counts per unit area) greatly differed between coated and uncoated substrates (cf. Fig. 6(b)). Fig. 6(g) and (h) show merged fluorescence images of Gla-osteocalcin (green) and osteopontin (red) as recorded for bone tissue grown on uncoated and Si_3N_4-coated Ti-alloy substrates, respectively. These data show that the bone tissue grown by cells on the uncoated Ti-alloy presented an unbalanced composition rich in osteopontin. Conversely, the bone tissue deposited on the Si_3N_4-coated Ti-alloy was richer in Gla-osteocalcin, with an osteocalcin/osteopontin balance resembling that of natural bone. This consistency between laser microscopy and biological assay data, shown in Fig. 6, substantiated the effect of the Si_3N_4 coating on Ti-alloy toward enhancing the osteogenic efficiency of human osteoblasts.

3.3. Antibacterial properties of Si_3N_4 coating

Fig. 7(a) and (b) show data representing the metabolic responses of Gram-positive *S. epidermidis* after exposure to uncoated and Si_3N_4-coated Ti6Al4V-alloy substrates in terms of optical density and fraction of dead bacteria, respectively. Cell viability data in (a), which are presented at the exposure times of 24 and 48 h, showed the existence of a larger population of bacteria on the uncoated substrate as compared to the Si_3N_4-coated one. A statistically validated decreasing trend for the bacterial population with time was detected on both substrates. However, the decrease rate was clearly higher for the Si_3N_4-coated substrate. Moreover, the fraction of dead bacteria at 48 h was negligible on the uncoated substrates, while almost the totality of bacteria underwent lysis on the Si_3N_4-coated substrates (Fig. 7(b)). DAPI (blue), CFDA (green), PI (red), and DAPI/CFDA/PI-merged fluorescence micrographs (taken at 48 h) clearly visualize the antibacterial performances of uncoated and Si_3N_4-coated substrates (in Fig. 7(c)~(f) and (g)~(j), respectively). Optical density data (in Fig. 7(e)) provide a direct assessment of the high efficacy of the Si_3N_4 coating in reducing bacterial adhesion. On the other hand, the significant difference seen in the density of red pixels (cf. Fig. 7(e) and (i) for uncoated and Si_3N_4-coated substrates, respectively) proves that the Si_3N_4 coating induced lysis in

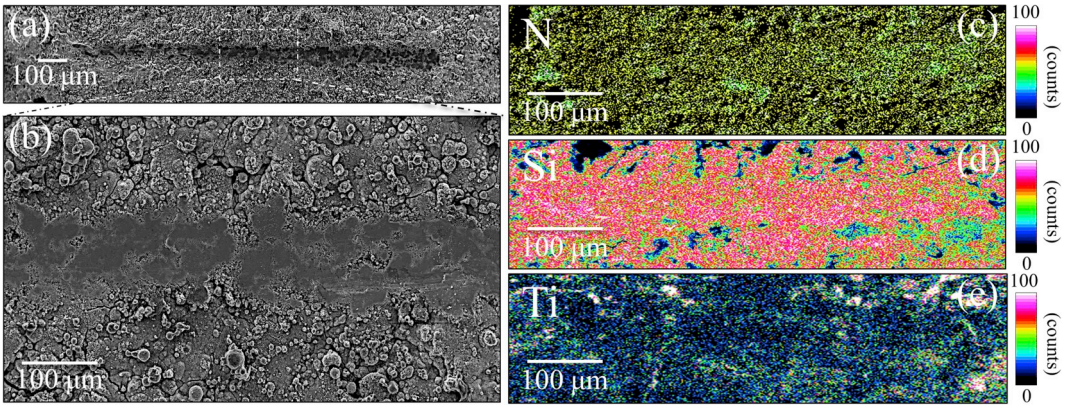

Fig. 5. Low (a) and high (b) magnification SEM micrographs taken at the site of a scratch test applied up to 25 N on the Si_3N_4-coated surface of Titanium substrate; EDS analyses are given in (b) and (c) for Si, and Ti elements, respectively.

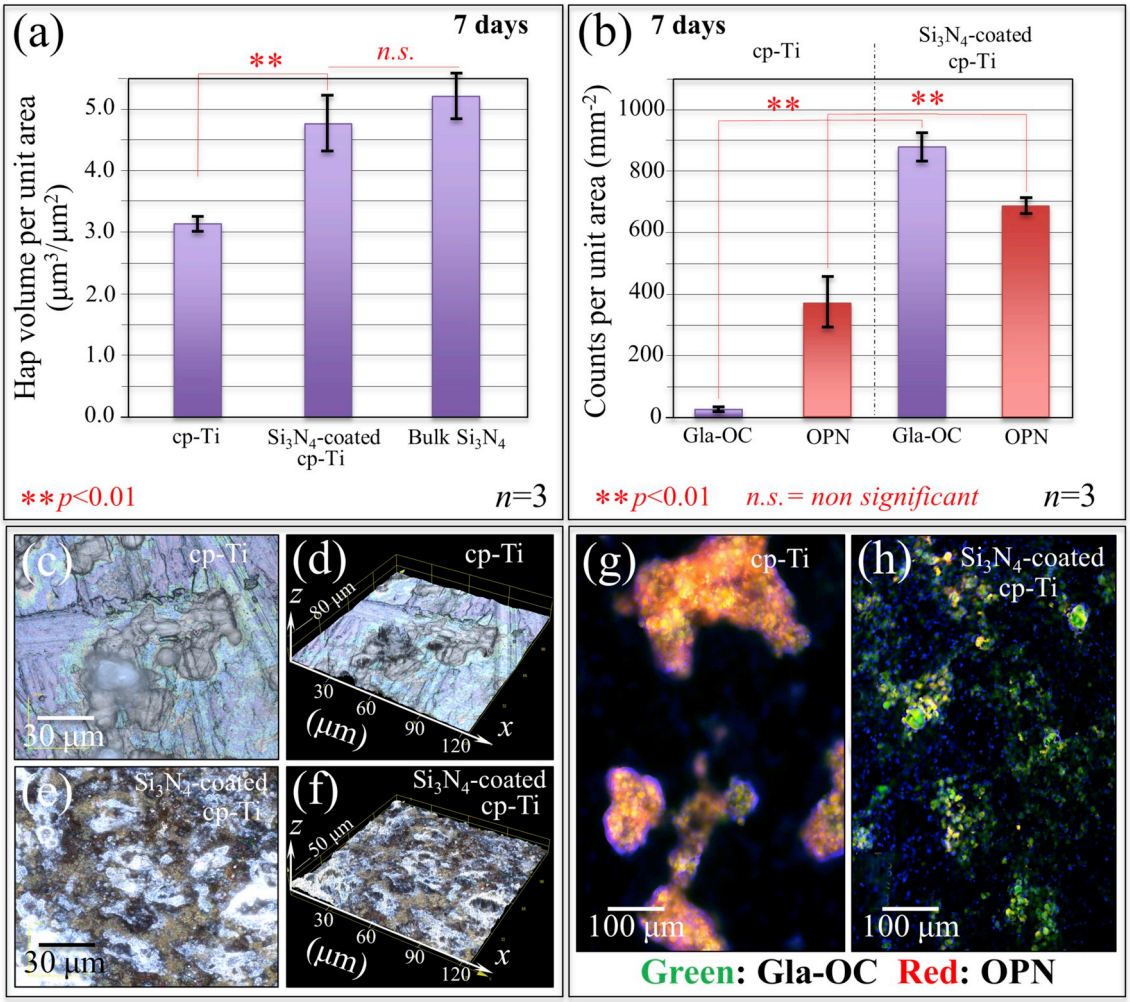

Fig. 6. Plots of (a) volumes of hydroxyapatite deposited by SaOS-2 cells per unit substrate area and (b) of their amounts of Gla-osteocalcin and osteopontin on Si_3N_4-coated and uncoated Titanium substrates (data statistically validated). Typical laser microscopy images that were employed in the volumetric laser-microscopy assessments are given for uncoated Titanium-alloy (planar and three-dimensional views in (c) and (d), respectively) and for Si_3N_4-coated Titanium substrates (planar and three-dimensional views in (e) and (f), respectively). In (g) and (h), merged fluorescence images of Gla-osteocalcin (green) and osteopontin (red) in bone tissue grown on uncoated Titanium and Si_3N_4-coated Titanium substrates, respectively. (For interpretation of the references to color in this figure legend, the reader is referred to the Web version of this article.)

Gram-positive *S. epidermidis*. Note that some antibacterial effect (although limited to a reduction in bacterial adhesion) was also found for the uncoated Ti-alloy sample. This effect is well-known and has been attributed to the presence of a TiO_2 passivation layer at the surface of the alloy (Kiwi et al., 2014; Vatansever et al., 2013). A rationale for the observed difference in antibacterial efficacy (i.e., related to the different chemical origins) between the Si_3N_4 coating and the TiO_2 passivation layer is addressed in the discussion section.

3.4. Application of the Si_3N_4-coating method to commercially available acetabular shells

In order to show the practical feasibility of our Si_3N_4 laser-deposition technology, we applied it to a commercially available porous Ti-alloy acetabular shell. The shells designed for cementless fixation to the human pelvis during total hip replacement, were coated with Si_3N_4 on their external, convex porous surface, which comes into direct contact with host bone after implantation. Fig. 8(a) and (b) show an uncoated and a Si_3N_4-coated acetabular shell, respectively. The coating procedure and the laser-sintering conditions were the same as those described in the previous sections. The selected Ti-alloy acetabular shells reflect a commercially successful design, manufactured with porous Ti-alloy, and optimized for rapid bone ingrowth (Kim and Yoo, 2016; Yamada et al., 2009; Epinette and Manley, 2008). The microstructures of uncoated and Si_3N_4-coated acetabular shells are shown in the high-resolution optical images of Fig. 8(c) and (d), respectively. The results of quantitative laser microscopy assessments on the structure of the porous shell before and after the Si_3N_4-coating procedure are shown in Fig. 8(e) and (f), respectively. Critically, from a commercial standpoint, and, as shown in these two latter figures (and from the related linear profiles shown at the bottom of each figure), the Ti-alloy surface preserved its mm-sized porous morphology even after deposition of the Si_3N_4 coating (i.e., our method did not disturb the favorable surface morphology of the convex, ingrowth surface of the cups).

Fig. 9(a) and (b) show the results of luciferin "glowing" experiments on Gram-negative *E. coli* bacteria-contaminated uncoated and Si_3N_4-coated Ti-alloy acetabular shells, respectively. The chemiluminescent oxyluciferin luciferase signal (recorded at 48 h) shows the difference in the degree of bacterial contamination between the acetabular shells *in toto*: the uncoated one was bright with fluorescent bacteria, while the coated one was essentially dark with a limited number of whitish spots. Such spots corresponded to microscopic areas in which the coating was not completely covering the internal side of the porosity (cf. the similarity in the whitish patterns of a poorly coated microscopic region and

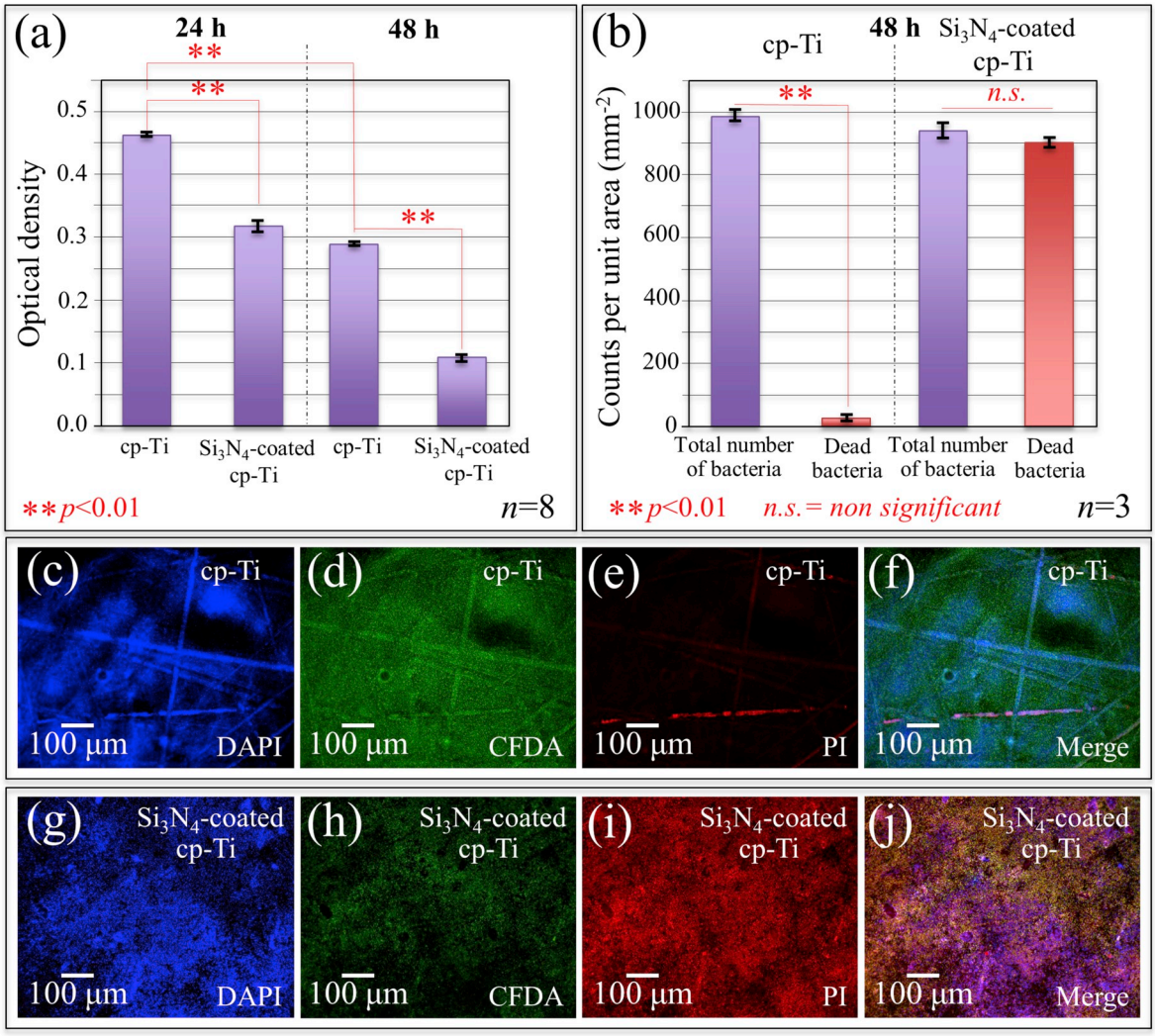

Fig. 7. Plots of (a) cell viability and (b) counts of dead/live Gram-positive *S. epidermidis* at 24 and 48 h for uncoated and Si_3N_4-coated Titanium substrates (data statistically validated); DAPI (blue), CFDA (green), PI (red), and DAPI/CFDA/PI-merged fluorescence micrographs (taken at 48 h) for uncoated ((c)~(f)) and Si_3N_4-coated substrates ((g)~(j)). (For interpretation of the references to color in this figure legend, the reader is referred to the Web version of this article.)

the microscopic bacterial enclaves in Fig. 9(c) and (d), respectively).

In sum, our work with commercially available acetabular shells not only demonstrated the practical feasibility of the Si_3N_4-coating laser technology on actual arthroplasty components, but also showed that the Si_3N_4 coating discouraged bacterial adhesion and proliferation.

4. Discussion

4.1. The common origin of osteogenic and antibacterial properties

It is well known that RNS such as N_2O, NO, and –OONO are well known to be highly effective biocidal agents (Fang, 1997; Sulemankhil et al., 2012; Seabra et al., 2016). A previous paper (Pezzotti, 2018) described the unique surface chemistry of bulk Si_3N_4 in terms of its capacity to be an exogenous NO donor. Spontaneous RNS elution from Si_3N_4 may discourage surface bacterial adhesion and activity. Unlike other direct eluting sources of exogenous NO, Si_3N_4 elutes mainly NH_4^+ and a small fraction of NH_3 ions at physiological pH, because of surface hydrolysis and homolytic cleavage of the Si–N covalent bond. Ammonium NH_4^+ can enter the cytoplasmic space of cells in controlled concentrations and through specific transporters (Knepper et al., 1989; Adeva et al., 2012), This ion is a nutrient used by cells to synthesize building-block proteins for enzymes and genetic compounds, thus sustaining cell differentiation and proliferation (Geisseler et al., 2010). Together with the leaching of orthosilicic acid and related compounds, NH_4^+ promotes osteoblast synthesis of bone tissue (Olkku and Mahonen, 2008; Aminian et al., 2011), and stimulates collagen type 1 synthesis in human osteoblasts (Aminian et al., 2011; Reffitt et al., 2003). Conversely, highly volatile ammonia NH_3 can freely penetrate the external membrane and directly target the stability of DNA/RNA structures in bacterial cells (Abumourad et al., 2012). The cellular toxicity of ammonia has been widely reported in a variety of contexts (Pezzotti, 2018; Marnett, 2000; Gerardi, 2006; Müller et al., 2006). However, the release of unpaired electrons from the mitochondria in eukaryotic cells activates a cascade of consecutive reactions, which starts with NH_3 oxidation into hydroxylamine NH_2OH (ammonia monooxygenase) along with an additional reductant contribution leading to further oxidation into NO_2^- nitrite through a process of hydroxylamine oxidoreductase (Pezzotti, 2018; Pacher et al., 2007; Arp and Stein, 2003; Stein and Yung, 2003). This latter process involves nitric oxide NO formation. The elution kinetics of such nitrogen species is slow but continuous, thus providing long-term efficacy against bacterial colonies including mutants (which, unlike eukaryotic cells, lack mitochondria). However, when slowly delivered, NO radicals have been shown to act in an efficient signaling pathway leading to enhanced differentiation and osteogenic activity of human osteoblasts (Pezzotti, 2018; Olkku and

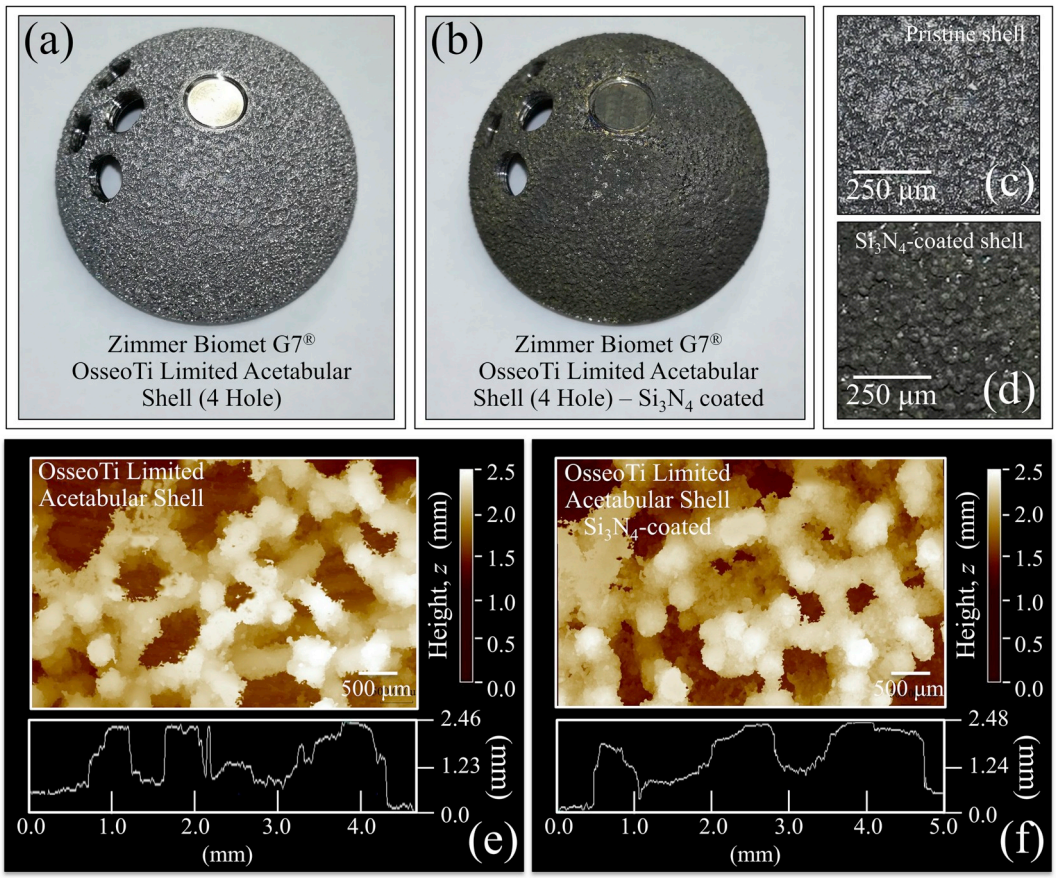

Fig. 8. Uncoated (a) and Si_3N_4-coated (b) Ti6Al4V acetabular shells specially designed with a porous surface for cementless hip arthroplasty; the microstructures of the uncoated and Si_3N_4-coated acetabular shells are shown at higher magnification in (c) and (d), respectively, as visualized by laser microscopy. The results of quantitative laser microscopy assessments on the structure of the porous structure of the shell before and after being coated with Si_3N_4 are shown in (e) and (f), respectively.

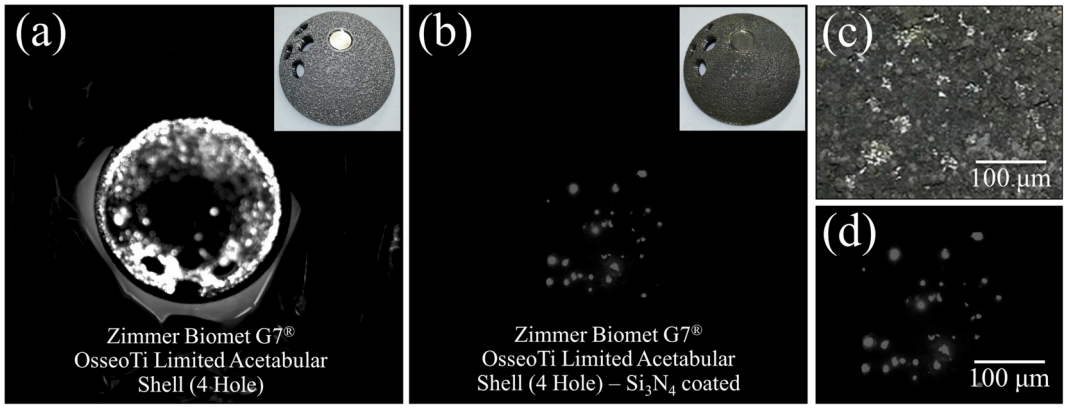

Fig. 9. Results of luciferin "glowing" experiments (at 48 h) conducted on Gram-negative *E. coli* bacteria-contaminated (a) uncoated and (b) Si_3N_4-coated Ti6Al4V acetabular shells. Observation of microscopic areas of incomplete coating are shown in (c) and (d).

Mahonen, 2008).

The Si_3N_4 coating showed concurrent osteogenic and antibacterial behaviors similar to those observed in bulk Si_3N_4 bioceramic implants. Fig. 10(a) and (b) schematically show the chemical interactions of mesenchymal cells and bacteria with the Si_3N_4 substrate, respectively. The present investigation shows that the dual behavior of the intrinsic surface chemistry of bulk Si_3N_4 can be replicated on Ti-alloy with a laser-deposited coating.

4.2. Comparison with other surface functionalization technologies

Other coating technologies have targeted antibacterial attributes in arthroplasty implants, and a classification has been proposed, as follows (Romanò et al., 2015): (i) Passive surface finishing or modification, in which passive coatings (i.e., not releasing bactericidal agents into the surrounding tissues) simply prevent or reduce bacterial adhesion through surface chemistry or structural modifications; (ii) Active surface finishing or modification, in which active coatings feature

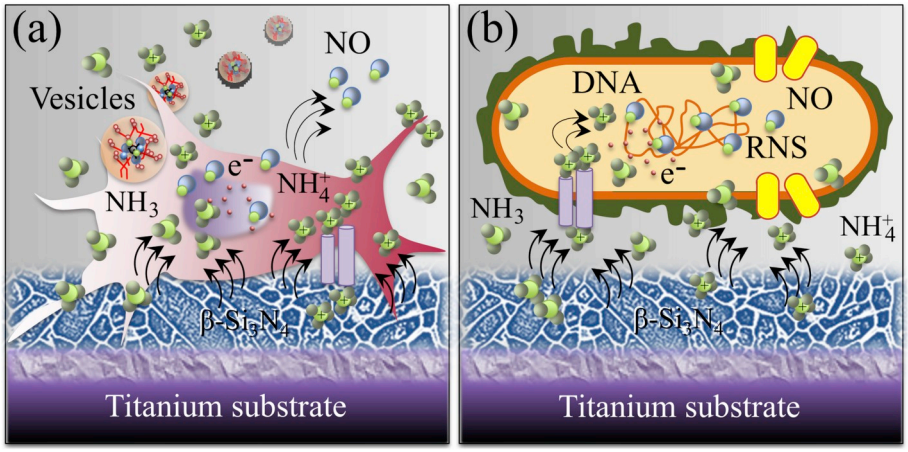

Fig. 10. Schematic draft of (a) osteoblast and (b) bacteria interactions at the biomolecular interface with Si_3N_4: eukaryotic cells use NH_4^+ molecules as a nutrient while being able to dissociate NH_3 to ultimately produce NO and use it as a signal for osteoblastogenesis; conversely, NH_3 is lethal to prokaryotic cells as it directly attacks its DNA/RNA structures.

pharmacologically active pre-incorporated bactericidal agents; and, (iii) Local carriers or coatings (biodegradable or not) that are applied at the time of the surgical procedure around the sample.

The bactericidal effect of Ti-alloy relies on a surface passivation layer, and thus falls into the above category (i) of "passive" coatings. Ultraviolet light irradiation (Gallardo-Moreno et al., 2009; Yu et al., 2003) and partial modification of the crystalline structure (from rutile into anatase phase) of the TiO_2 surface oxide layer (Del Curto et al., 2005) can inhibit bacterial adhesion without compromising osteogenesis on titanium alloy implants. Both are relevant to the acetabular shells investigated in the present study, since the shells possessed a fraction of anatase phase in their passivation layer, and were UV irradiated for sterilization prior to bacterial testing.

The ability of the Ti-alloy passivation layer to resist bacterial adhesion is limited, and depends on the bacterial species and loads (Hetrick and Schoenfisch, 2006). Moreover, the long-term effects on the osteogenic behavior of host cells remains a point of concern due to the release of metallic ions, as predicted by early *in vitro* studies (Thompson and Puleo, 1996; Puleo and Huh, 1995), and demonstrated by fibrosis effects observed in the periprosthetic tissue of osteolytic implants (Marin et al., 2010; Chassot et al., 2004; Apostu et al., 2018), as well as by recently reported adverse effects in dental implants (http://www.kokusen.go.jp/, 2019). Our experiments confirmed the efficacy of the Ti-alloy passivation layer against Gram-positive *S. epidermidis* but also a lesser effectiveness against Gram-negative *E coli* (cf. Figs. 7 and 9). In addition, Ti-alloy showed relatively poor *in vitro* osteoblast activity observed on flat substrates and the quality parameter of the deposited bony tissue (cf. Fig. 6).

Regarding the above category (ii), a number of different coatings have been proposed that could release (pre-incorporated) pharmacologically active bactericidal agents, such as metallic ions (e.g., silver, copper, or zinc) (Noda et al., 2009; Panacek et al., 2009; Wafa et al., 2015; Hardes et al., 2010; Grass et al., 2011; Petrini et al., 2006; Hodgkinson and Petris, 2012), non-metallic ions (e.g., iodine or selenium) (Tsuchiya et al., 2012; Holinka et al., 2013), and organic molecules (e.g., antibiotics, anti-infective peptides, and nitric oxide) (Guillaume et al., 2012; Tang et al., 2012; Fuchs et al., 2011; Yount and Yeaman, 2012a; Haney and Hancock, 2013; Holmberg et al., 2013; Reger et al., 2017). The limiting factor in these approaches is related to the cytotoxicity of released ions toward bone cells (Romanò et al., 2015). Coatings capable to release organic molecules such as antibiotics, peptides, and nitric oxide may also be effective against a wide range of pathogens (Yount and Yeaman, 2012b). However, this approach is limited by the limited duration of efficacy and unpredictable elution kinetics of the pharmacologically active agents (Wen et al., 2015). The reliance on released doses of antibiotics also invokes concerns regarding the possible induction of bacterial resistance.

Bacterial resistance develops less frequently in antimicrobial peptides than in antibiotics (Dobson et al., 2013), and metal alloys surfaces functionalized with antimicrobial peptides have shown excellent antibacterial effects against the typical arthroplasty pathogens (Holmberg et al., 2013). The systemic effects of these substances in the human body are poorly understood and require further investigations before clinical applications.

Reger et al. (2017) succeeded in functionalizing the surface of Ti6Al4V with a *S*-nitrosothiol NO donor using self-assembled monolayers. This procedure resulted in NO release in the order of the hundredths of nmol/cm^2 under physiological conditions. Such surface functionalization restrained the growth of both *S. epidermidis* and *E. coli* bacterial strains. Note that the NO functionalizing molecules could exogenously activate osteoblastogenesis and in low doses are not cytotoxic (Felka et al., 2014; Abnosi and Pari, 2019). However, the applicability of this approach to the porous surface of cementless prostheses and a full control of the NO-release kinetics *in vivo* yet remains unclear.

Si_3N_4 coating on Ti-alloy may confer resistance against adhesion of both Gram-positive and Gram-negative bacteria, while stimulating osteoblasts to deposit more bone tissue, and of higher quality. Unlike other NO donors, the Si_3N_4 coating released the nitrogen radical steadily, with a favorable kinetics.

5. Conclusion

A 3D-laser-sintering manufacturing process deposited a dense, tenaciously adherent Si_3N_4 coating (with thickness 10–20 μm) onto the porous T-alloy surface of commercially available acetabular components. This technology may achieve rapid osseous fixation, while resisting bacteria. Competing technologies have addressed either periprosthetic infections of enhanced osteogenesis, but not both (Raphel et al., 2016). The dual benefits of a Si_3N_4 coating relate to its RNS surface chemistry, and slow kinetics that favor osseointegration, while inhibiting bacteria. Further studies are needed to establish if Si_3N_4 may offer clinically relevant advantages over the commonly used hydroxyapatite coatings on uncemented arthroplasty implants used today.

Declaration of competing interest

Giuseppe Pezzotti is a consultant to SINTx Technologies Corporation. Bryan J. McEntire and B. Sonny Bal work at SINTx Technologies Corporation.

Acknowledgements

We are grateful to Dr. Nagayama of Kyoto Municipal Institute of Industrial Technology and Culture for generating confocal microscopy imaging. This work was supported by KAKENHI (Grant in Aid for Scientific Research C 17K01389).

References

Abnosi, M.H., Pari, S., 2019. Exogenous nitric oxide induced early mineralization in rat bone marrow mesenchymal stem cells via activation of alkaline phosphatase. Iran. Biomed. J. 23, 142–152.
Abumourad, I.M.K., Hanna, M.I., Girgis, S.M., 2012. Genotoxicity assessment of ammonia in cultured *Oreochromis niloticus* using RAPD assay. J Genet Eng Biotechnol 10, 209–212.
Adeva, M.M., Souto, G., Blanco, N., Donapetry, C., 2012. Ammonium metabolism in humans. Metabolism 61, 1495–1511.
Aminian, A., Solati-Hashjin, M., Samadikuchaksaraei, A., Bakhshi, F., Gorjipour, F., Farzadi, A., et al., 2011. Synthesis of silicon-substituted hydroxyapatite by a hydrothermal method with two different phosphorous sources. Ceram. Int. 37, 1219–1229.
Anselme, K., 2000. Osteoblast adhesion on biomaterials. Biomaterials 21, 667–681.
Apostu, D., Lucaciu, O., Berce, C., Lucaciu, D., Cosma, D., 2018. Current methods of preventing aseptic loosening and improving osseointegration of titanium implants in cementless hip arthroplasty: a review. J. Int. Med. Res. 46, 2104–2119.
Arp, D.J., Stein, L.Y., 2003. Metabolism of inorganic N compounds by ammonia-oxidizing bacteria. Crit. Rev. Biochem. Mol. Biol. 38, 471–495.
Ball, H.T., McEntire, B., Bal, B.S., 2017. Accelerated cervical fusion of silicon nitride versus PEEK spacers: a comparative clinical study. J. Spine 6, 396.
Canadian Institute for Health Information, 2018. Hip and Knee Replacements in Canada, 2016–2017: Canadian Joint Replacement Registry Annual Report. CIHI, Ottawa, ON.
Chassot, E., Irigaray, J.L., Terver, S., Vanneuville, G., 2004. Contamination by metallic elements released from joint prostheses. Med. Eng. Phys. 26, 193–199.
Del Curto, B., Brunella, M.F., Giordano, C., Pedeferri, M.P., Valtulina, V., Visai, L., et al., 2005. Decreased bacterial adhesion to surface-treated titanium. Int. J. Artif. Organs 28, 718–730.
Dobson, A.J., Purves, J., Kamysz, W., Rolff, J., 2013. Comparing selection on *S. aureus* between antimicrobial peptides and common antibiotics. PLoS One 8, e76521.
Engesæter, L.B., Espehaug, B., Lie, S.A., Furnes, O., Havelin, L.I., 2006. Does cement increase the risk of infection in primary total hip arthroplasty? Revision rates in 56,275 cemented and uncemented primary THAs followed for 0-16 years in the Norwegian Arthroplasty Register. Acta Orthop. 77, 351–358.
Epinette, J.A., Manley, M.T., 2008. Uncemented stems in hip replacement - hydroxyapatite or plain porous: does it matter? Based on a prospective study of HA Omnifit stems at 15-years minimum follow-up. Hip Int. 18, 69–74.
Fang, F.C., 1997. Perspectives series: host/pathogen interactions. Mechanisms of nitric oxide-related antimicrobial activity. J. Clin. Investig. 99, 2818–2825.
Felka, T., Ulrich, C., Rolauffs, B., Mittag, F., Kluba, T., DeZwart, P., Ochs, Gunnar, Bonin, M., Nieselt, K., Hart, M.L., Aicher, W.K., 2014. Nitric oxide activates signaling by c- Raf, MEK, p-JNK, p38 MAPK and p53 in human mesenchymal stromal cells and inhibits their osteogenic differentiation by blocking expression of Runx 2. J. Stem Cell Res. Ther. 4, 195.
Fuchs, T., Stange, R., Shmidmaier, S., Raschke, M.J., 2011. The use of gentamicin-coated nails in the tibia: preliminary results of a prospective study. Arch. Orthop. Trauma Surg. 131, 1419–1425.
Gallardo-Moreno, A.M., Pacha-Olivenza, M.A., Saldana, L., Perez-Giraldo, C., Bruque, J. M., Vilaboa, N., et al., 2009. *In vitro* biocompatibility and bacterial adhesion of physico-chemically modified Ti6Al4V surface by means of UV irradiation. Acta Biomater. 5, 181–192.
Geisseler, D., Horwath, W.R., Joergensen, R.G., Ludwig, B., 2010. Pathways of nitrogen utilization by soil microorganisms - Areview. Soil Biol. Biochem. 42, 2058–2067.
Gerardi, M.H., 2006. Wastewater Bacteria, vol. 14. John Wiley & Sons, Inc, Hoboken, NJ USA.
Grass, G., Rensing, C., Solioz, M., 2011. Metallic copper as an antimicrobial surface. Appl. Environ. Microbiol. 77, 1541–1547.
Guillaume, O., Garric, X., Lavigne, J.P., Van Den Berghe, H., Coudane, J., 2012. Multilayer, degradable coating as a carrier for the sustained release of antibiotics: preparation and antimicrobial efficacy in vitro. J. Control. Release 162, 492–501.
Hailer, N.P., Garellick, G., Kärrholm, J., 2010. Uncemented and cemented primary total hip arthroplasty in the Swedish Hip Arthroplasty Register. Acta Orthop. 81, 34–41.
Haney, E.F., Hancock, R.E., 2013. Peptide design for antimicrobial and immunomodulatory applications. Biopolymers 100, 572–583.
Hardes, J., von Eiff, C., Streitbuerger, A., Balke, M., Budny, T., Henrichs, M.P., et al., 2010. Reduction of periprosthetic infection with silver-coated megaprostheses in patients with bone sarcoma. J. Surg. Oncol. 101, 389–395.
Hetrick, E.M., Schoenfisch, M.H., 2006. Reducing implant-related infections: active release strategies. Chem. Soc. Rev. 35, 780–789.
Hirakawa, K., Mori, M., Yoshida, M., Oikawa, S., Kawanishi, S., 2004. Photo-irradiated titanium dioxide catalyzes site specific DNA damage via generation of hydrogen peroxide. Free Radic. Res. 38, 439–447.
Hodgkinson, V., Petris, M.J., 2012. Copper homeostasis at the host-pathogen interface. J. Biol. Chem. 287, 13549–13555.
Holinka, J., Pilz, M., Kubista, B., Presterl, E., Windhager, R., 2013. Effects of selenium coating of orthopaedic implant surfaces on bacterial adherence and osteoblastic cell growth. Bone Joint Lett. J 95, 678–682.
Holmberg, K.V., Abdolhosseini, M., Li, Y., Chen, X., Gorr, S.U., Aparicio, C., 2013. Bio-inspired stable antimicrobial peptide coatings for dental applications. Acta Biomater. 9, 8224–8231.
Homsy, C.A., Cain, T.E., Kessler, F.B., Anderson, M.S., King, J.W., 1972. Porous implant systems for prosthesis stabilization. Clin. Orthop. Relat. Res. 89, 220–235.
http://www.kokusen.go.jp/pdf/n-20190314_1.pdf downloaded on May 4th 2019.
Karuppal, R., 2016. Biological fixation of total hip arthroplasty: facts and factors. J. Orthop. 13, 190–192.
Kim, J.T., Yoo, J.J., 2016. Implant design in cementless hip arthroplasty. Hip Pelvis 28, 65–75.
Kiwi, J., Rtimi, S., Sanjines, R., Pulgarin, C., 2014. TiO_2 and TiO_2-doped films able to kill bacteria by contact: new evidence for the dynamics of bacterial inactivation in the dark and under light irradiation. Int. J. Photoenergy 2014, 17, 785037.
Knepper, M.A., Packer, R., Good, D.W., 1989. Ammonium transport in the kidney. Physiol. Rev. 69, 179–249.
Lucht, U., 2000. The Danish Hip arthroplasty register. Acta Orthop. Scand. 71, 433–439.
Maness, P.C., Smolinski, S., Blake, D.M., et al., 1999. Bactericidal activity of photocatalytic $TiO_{(2)}$ reaction: toward an understanding of its killing mechanism. Appl. Environ. Microbiol. 65, 4094–4098.
Marin, E., Fusi, S., Pressacco, M., Paussa, L., Fedrizzi, L., 2010. Characterization of cellular solids in Ti6Al4V for orthopaedic implant applications: trabecular titanium. J. Mech. Behav. Biomed. Mater. 3, 373–381.
Marnett, L.J., 2000. Oxyradicals and DNA damage. Carcinogenesis 21, 361–370.
McEntire, B., Lakshminarayanan, R., Thirugnanasambandam, P., Seitz-Sampson, J., Bock, R., O'Brien, D., 2016. Processing and characterization of silicon nitride bioceramics. Bioceram. Dev. Appl. 6 (1).
Müller, T., Walter, B., Wirtz, A., Burkovski, A., 2006. Ammonium toxicity in bacteria. Curr. Microbiol. 52, 400–406.
Noda, I., Miyaji, F., Ando, Y., Miyamoto, H., Shimazaki, T., Yonekura, Y., et al., 2009. Development of novel thermal sprayed antibacterial coating and evaluation of release properties of silver ions. J. Biomed. Mater. Res. B Appl. Biomater. 89, 456–465.
Olkku, A., Mahonen, A., 2008. Wnt and steroid pathways control glutamate signalling by regulating glutamine synthetase activity in osteoblastic cells. Bone 43, 483–493.
Pacher, P., Beckman, J.S., Liaudet, L., 2007. Nitric Oxide and peroxynitrite in health and disease. Physiol. Rev. 87, 315–424.
Panacek, A., Kolar, M., Vecerova, R., Prucek, R., Soukupova, J., Krystof, V., et al., 2009. Antifungal activity of silver nanoparticles against Candida spp. Biomaterials 30, 6333–6340.
Petrini, P., Arciola, C.R., Pezzali, I., Bozzini, S., Montanaro, L., Tanzi, M.C., et al., 2006. Antibacterial activity of zinc modified titanium oxide surface. Int. J. Artif. Organs 29, 434–442.
Pezzotti, G., 2018. A spontaneous solid-state NO donor to fight antibiotic resistant bacteria. Mater Today Chem 9, 1–11.
Pezzotti, G., McEntire, B.J., Bock, R., Boffelli, M., Zhu, W., Vitale, E., Puppulin, L., Adachi, T., Yamamoto, T., Kanamura, N., Bal, B.S., 2016. Silicon nitride: a synthetic mineral for vertebrate biology. Sci. Rep. 6, 31717.
Pezzotti, G., McEntire, B.J., Bock, R., Zhu, W., Boschetto, F., Rondinella, A., Marin, E., Marunaka, Y., Adachi, T., Yamamoto, T., Kanamura, N., Bal, B.S., 2016. ACS Biomater. Sci. Eng. 2, 1121–1134.
Pezzotti, G., Bock, R.M., McEntire, B.J., Jones, E., Boffelli, M., Zhu, W., et al., 2016. Silicon nitride bioceramics induce chemically driven lysis in *Porphyromonas gingivalis*. Langmuir 32, 3024–3035.
Pezzotti, G., 2019. Silicon nitride: A bioceramic with a gift. ACS Appl. Mater. Interfaces 11 (30), 26619–26636.
Pezzotti, G., Bock, R.M., Adachi, T., Rondinella, A., Boschetto, F., Zhu, W., Marin, E., McEntire, B.J., Bal, B.S., Mazda, O., 2017. Silicon nitride surface chemistry: a potent regulator of mesenchymal progenitor cell activity in bone formation. Appl Mater Today 9, 82–95.
Pezzotti, G., Marin, E., Adachi, T., Rondinella, A., Boschetto, F., Zhu, W., Sugano, N., Bock, R.M., McEntire, B., Bal, B.S., 2017. Bioactive silicon nitride: a new therapeutic material for osteoarthropathy. Sci. Rep. 7, 44848.
Pezzotti, G., Oba, N., Zhu, W., Marin, E., Rondinella, A., Boschetto, F., McEntire, B., Yamamoto, K., Bal, B.S., 2017. Human osteoblasts grow transitional Si/N apatite in quickly osseointegrated Si_3N_4 cervical insert. Acta Biomater. 64, 411–420.
Pezzotti, G., Bock, R.M., McEntire, B.J., Adachi, T., Marin, E., Boschetto, F., et al., 2018. *In vitro* antibacterial activity of oxide and non-oxide bioceramics for arthroplastic devices: I. *In situ* time-lapse Raman spectroscopy. Analyst 143, 3708–3721.
Puleo, D.A., Huh, W.W., 1995. Acute toxicity of metal ions in cultures of osteogenic cells derived from bone marrow stromal cells. J. Appl. Biomater. 6, 249–258.
Puolakka, T.J., Pajamaki, K.J., Halonen, P.J., et al., 2001. The Finnish Arthroplasty Register: report of the hip register. Acta Orthop. Scand. 72, 433–441.
Rambo, W.M., 2018. Treatment of lumbar discitis using silicon nitride spinal spacers: a case series and literature review. Int J Surg Case Rep 43, 61–68.
Raphel, J., Holodniy, M., Goodman, S.B., Heilshorn, S.C., 2016. In: Multifunctional Coatings to Simultaneously Promote Osseointegration and Prevent Infection Oforthopaedic Implants, vol. 84, pp. 301–314.
Reffitt, D.M., Ogston, N., Jugdaohsingh, R., Cheung, H.F.J., Evans, B.A.J., Thompson, R. P.H., et al., 2003. Orthosilicic acid stimulates collagen type 1 synthesis and osteoblastic differentiation in human osteoblast-like cells in vitro. Bone 32, 127–135.
Reger, N.A., Meng, W.S., Gawalt, E.S., 2017. Antimicrobial activity of nitric oxide-releasing Ti-6Al-4V metal oxide. J. Funct. Biomater. 21, 20.

Romanò, C.L., Scarponi, S., Gallazzi, E., Romanò, D., Drago, L., 2015. Antibacterial coating of implants in orthopaedics and trauma: a classification proposal in an evolving panorama. J. Orthop. Surg. Res. 10, 157.
Seabra, A.B., Pelegrino, M.T., Haddad, P.S., 2016. Can nitric oxide overcome bacterial resistance to antibiotics? In: Kon, K., Rai, M. (Eds.), Antibiotic Resistance: Mechanisms and New Antimicrobial Approaches. Academic Press, London, UK, pp. 187–204.
Smith, M.W., Romano, D.R., McEntire, B.J., Bal, B.S., 2018. A single center retrospective clinical evaluation of anterior cervical discectomy and fusion comparing allograft spacers to silicon nitride cages. J Spine Surg 4, 349–360.
Stein, L.Y., Yung, Y.L., 2003. Production, Isotopic composition, and atmospheric fate of biologically produced nitrous oxide. Annu. Rev. Earth Planet Sci. 31, 329–356.
Sulemankhil, I., Ganopolsky, J.G., Dieni, C.A., Dan, A.F., Jones, M.L., Prakash, S., 2012. Prevention and treatment of virulent bacterial biofilms with an enzymatic nitric oxide-releasing dressing. Antimicrob. Agents Chemother. 56, 6095–6103.
Tang, Y., Zhao, Y., Wang, H., Gao, Y., Liu, X., Wang, X., et al., 2012. Layer-by-layer assembly of antibacterial coating on interbonded 3D fibrous scaffolds and its cytocompatibility assessment. J. Biomed. Mater. Res. A 100, 2071–2078.
Thompson, G.J., Puleo, D.A., 1996. Ti-6Al-4V ion solution inhibition of osteogenic cell phenotype as a function of differentiation timecourse *in vitro*. Biomaterials 17, 1949–1954.
Tsuchiya, H., Shirai, T., Nishida, H., Murakami, H., Kabata, T., Yamamoto, N., et al., 2012. Innovative antimicrobial coating of titanium implants with iodine. J. Orthop. Sci. 17, 595–604.
Vatansever, F., de Melo, W.C.M.A., Avci, P., Vecchio, D., Sadasivam, M., Gupta, A., Chandran, R., Karimi, M., Parizotto, N.A., Yin, R., Tegos, G.P., Hamblin, M.R., 2013. Antimicrobial strategies centered around reactive oxygen species - bactericidal antibiotics, photodynamic therapy and beyond. FEMS Microbiol. Rev. 37, 955–989.
Wafa, H., Grimer, R.J., Reddy, K., Jeys, L., Abudu, A., Carter, S.R., et al., 2015. Retrospective evaluation of the incidence of early periprosthetic infection with silver-treated endoprostheses in high-risk patients: case–control study. Bone Joint Lett. J 97B, 252–257.
Wang, W., Poh, C.K., 2013. Titanium alloys in orthopaedics. In: Sieniawski, J., Ziaja, W. (Eds.), Advances in Properties Control (IntechOpen).
Webster, T.J., Patel, A.A., Rahaman, M.N., Bal, B.S., 2012. Anti-infective and osteointegration properties of silicon nitride, poly(ether ether ketone), and titanium implants. Acta Biomater. 8, 4447–4454.
Wen, H., Jung, H., Li, X., 2015. Drug delivery approaches in addressing clinical pharmacology-related issues: opportunities and challenges. AAPS J. 17, 1327–1340.
Yamada, H., Yoshihara, Y., Henmi, O., Morita, M., Shiromoto, Y., Kawano, T., Kanaji, A., Ando, K., Nakagawa, M., Kosaki, N., Fukaya, E., 2009. Cementless total hip replacement: past, present, and future. J. Orthop. Sci. 14, 228–241.
Yount, N.Y., Yeaman, M.R., 2012. Emerging themes and therapeutic prospects for anti-infective peptides. Annu. Rev. Pharmacol. Toxicol. 52, 337–360.
Yount, N.Y., Yeaman, M.R., 2012. Emerging themes and therapeutic prospects for anti-infective peptides. Annu. Rev. Pharmacol. Toxicol. 52, 337–360.
Yu, J.C., Ho, W., Lin, J., Yip, H., Wong, P.K., 2003. Photocatalytic activity, antibacterial effect, and photoinduced hydrophilicity of TiO2 films coated on a stainless steel substrate. Environ. Sci. Technol. 37, 2296–2301.